Micromechanical Disk Array for Enhanced Frequency Stability Against Bias Voltage Fluctuations

Lingqi Wu

Electrical Engineering and Computer Sciences
University of California at Berkeley

Technical Report No. UCB/EECS-2014-182
http://www.eecs.berkeley.edu/Pubs/TechRpts/2014/EECS-2014-182.html

November 20, 2014

Micromechanical Disk Array for Enhanced Frequency Stability Against Bias Voltage Fluctuations

by

Lingqi Wu

A report submitted in partial satisfaction of the

requirements for the degree of

Master of Science

in

Engineering – Electrical Engineering and Computer Sciences

in the

Graduate Division

of the

University of California, Berkeley

Committee in charge:

Professor Clark T.-C. Nguyen, Chair

Professor Liwei Lin

Fall 2014

Micromechanical Disk Array for Enhanced Frequency Stability Against Bias Voltage Fluctuations

by

Lingqi Wu

Research Project

Submitted to the Department of Electrical Engineering and Computer Sciences, University of California at Berkeley, in partial satisfaction of the requirements for the degree of **Master of Science, Plan II**.

Approval for the Report and Comprehensive Examination:

Committee:

Professor Clark T.-C. Nguyen
Research Advisor

(Date)

* * * * * * *

Professor Liwei Lin
Second Reader

(Date)

Micromechanical Disk Array for Enhanced Frequency Stability Against Bias Voltage Fluctuations

Abstract

Micromechanical Disk Array for Enhanced Frequency Stability Against Bias Voltage Fluctuations

by

Lingqi Wu

Master of Science in Electrical Engineering and Computer Sciences

University of California, Berkeley

Professor Clark T.-C. Nguyen, Chair

High-Q capacitive-gap transduced micromechanical resonators constructed via MEMS technology have recently taken center-stage among potential next generation timing and frequency reference devices that might satisfy present and future applications. Notably, oscillators referenced to very high Q capacitive-gap transduced MEMS resonators have already made inroads into the low-end timing market, and research devices have been reported to satisfy GSM phase noise requirements while only consuming less than 80 μW of power. Meanwhile, such devices have also posted some impressively low acceleration sensitivities, with measured sensitivity vectors less than 0.5 ppb/g.

Interestingly, theory predicts that the acceleration sensitivity of these devices should be even better than this, if not for frequency instability due to electrical stiffness. Indeed, electrical stiffness is predicted to set lower limits on not only short-term stability, but long-term as well, especially when one considers frequency variations due to charging or temperature-induced geometric shifts.

Pursuant to circumventing electrical stiffness-based instability, this work introduces a more circuit design-friendly equivalent circuit model that uses negative capacitance to capture the influence of electrical stiffness on device and circuit behavior. This new circuit model reveals that capacitive-gap transduced micromechanical resonators can offer better stability against electrical-stiffness-based frequency instability when used in large mechanically-coupled arrays. Measurements confirm that a 215-MHz 50-resonator disk array achieves a 3.5× enhancement in frequency stability against dc-bias voltage variation over a stand-alone single disk counterpart. The new equivalent circuit predicts the measurement data and its trends quite well, creating good confidence for using this circuit to guide new oscillator and filter designs that, depending on the application, can enhance or suppress electrical stiffness.

_____

Professor Clark T.-C. Nguyen
Research Advisor

To my parents and Fangran

纪念我的奶奶 杨秀英 (1935-2014)

TABLE OF CONTENTS

List of Figures ..... **iii**

List of Tables ..... **v**

Acknowledgments ..... **vi**

Chapter 1 Introduction **1**

1.1. Motivation: Frequency Stability Enhancement for Oscillators 1
1.2. Capacitive-gap Transduced Radial Contour Mode Disk Resonators 3
1.3. Traditional Equivalent Circuit 4
1.3.1. Core *lcr* Tank 5
1.3.2. Electromechanical Coupling Factor η_{ei} 6
1.3.3. Frequency Pulling Effect from Electrical Stiffness k_e 7
1.4. Outline 8

Chapter 2 Negative Capacitance Based Equivalent Circuit Model **9**

2.1. Limitations of Traditional Equivalent Circuit 9
2.2. Negative Capacitance Equivalent Circuit 10
2.3. Mitigation of Electrical Stiffness 11

Chapter 3 Micromechanical Disk Array Composite **13**

3.1. Schematic of a Radial Contour Mode Disk Array Composite 13
3.2. Frequency Stability Enhancement of a Disk Array Composite 16
3.3. Design Example 17
3.4. Fabrication Process 18

Chapter 4 Measurement Results **20**

4.1. Frequency Stability Against DC-bias Voltages 20
4.2. Motional Resistance 22

Chapter 5 Conclusions **24**

5.1. Impact on Applications 24
5.2. Conclusion 25

Bibliography **26**

List of Figures

Figure 1.1. A 61-MHz Pierce oscillator referenced to a capacitive-gap transduced wine glass disk resonator with its phase noise performance making the GSM specifications. 1

Figure 1.2. Various factors that can contribute to electrical stiffness induced frequency instability, which includes bias voltage noise, environment vibration, dielectric charging, and temperature drift. 2

Figure 1.3. *Q* Comparison between a capacitive-gap transduced disk resonator and a piezoelectric ring resonator at similar resonance frequencies. 3

Figure 1.4. (a) Schematic of a capacitive-gap transduced all-polysilicon radial contour mode disk resonator in a two-port excitation and sensing configuration; (b) Finite element simulation of radial contour mode shape. 4

Figure 1.5. Classic equivalent electrical circuit for a capacitive gap micromechanical disk resonator with electrical stiffness lumped into the variable capacitance c_r. 5

Figure 2.1. Negative capacitance equivalent circuit of a two-port micromechanical radial contour mode disk resonator. Here, the new equivalent circuit uses a negative capacitance exactly equal in magnitude to the shunt static electrode-to-resonator overlap capacitance C_{oi} at each electrode terminal to capture the electrical stiffness induced frequency shift. 10

Figure 2.2. Negative capacitance small-signal equivalent circuits for a two-port capacitive-gap micromechanical contour mode disk resonator: (a) Negative capacitance equivalent circuit with electrical stiffness separated from mechanical stiffness. (b) Negative capacitance equivalent circuit with electrical stiffness reflected through transformers to outside the core *lcr* loop. .. 11

Figure 3.1. (a) Schematic of a radial contour mode disk array-composite with disks linked by λ/2 coupling beams to enforce in phase vibration of each individual resonator. (b) Simulated modal depiction of a 3-resonator disk array with all disks vibrating in phase in radial-contour mode shapes. 13

Figure 3.2. FEA simulated mode shapes of a mechanically coupled three-resonator radial contour mode disk array. 14

Figure 3.3. Two-port modeling of a mechanical acoustic coupling beam in analogy to an electrical transmission line. 15

Figure 3.4. T-network modeling of a mechanical acoustic coupling beam with the force (F_i) in analogy to a voltage in electrical domain and the velocity (X_i) in analogy to a current in electrical domain. 15

Figure 3.5. (a) Negative capacitance equivalent circuit of a disk array–composite. With only the in-phase mode selected, the structure practically behaves like a single resonator, making it share the same equivalent circuit topology as a single disk resonator. (b) Negative capacitance

equivalent circuit of a disk array with *N* resonators based on element values in the single resonator equivalent circuit in Figure 2.2(b) 16

Figure 3.6. Cross-sections showing the last few steps in the fabrication process for a 215-MHz all-polysilicon disk resonators with CMPed electrodes (a. b), and a comparison to previous work's fabrication process, (c). 19

Figure 3.7. SEM of a 215-MHZ 50nm capacitive-gap contour mode disk array employing 16 resonators..... 19

Figure 3.8. SEM of a 215-MHZ 50nm capacitive-gap contour mode disk array employing 50 resonators..... 19

Figure 4.1. S21 direct measurement setup for a polysilicon 215-MHz capacitive-gap radial-contour mode disk resonator. 20

Figure 4.2. Frequency spectrum of a single radial contour mode disk resonator under different dc-bias voltage conditions. (V_P = 5 V, 10 V, and 15 V)..... 21

Figure 4.3. Measured curves of resonance frequency versus dc-bias voltage V_P plotted against simulation using negative capacitance equivalent circuit models for disk arrays with N=1, N=8, N=16, and N=50. 21

Figure 4.4. Frequency spectrum comparison of a 50-resonator radial contour mode disk array with a single disk resonator, both are measured with same dc-bias voltage. 23

LIST OF TABLES

Table I: Radial contour mode disk array design equations and procedure summary 17

Table II: Comparison of design variables and equivalent circuit element values for 215-MHz radial contour mode disk arrays with different number of mechanically-coupled resonators. 18

Table III: Electrode-to-resonator overlap capacitance and trace resistances for radial contour mode disk array with different number of resonators..... 22

ACKNOWLEDGEMENTS

I would like to express my sincere gratitude to my advisor Professor Clark T.-C. Nguyen for his professional guidance and encouragement throughout my research. It is my honor to join his research group in Berkeley Sensor and Actuator Center (BSAC) as a graduate student researcher. His invaluable advice on my research truly inspires me. I have always admired his vast knowledge of MEMS, charismatic leadership, and sense of humor.

I would also like to thank Professor Liwei Lin for reading this research report. His course ME219 (Parametric and Optimal Design of MEMS) offered me a lot of insightful ideas to optimize the performance of capacitive-gap transduced resonators.

I am also very grateful to all my colleagues in Prof. Clark Nguyen's research group. It has been a pleasure to work with all of them. Especially, I would like to thank Zeying Ren for her help on fabricating the devices. She gave me a lot of advice on MEMS fabrication and her rich experience in microfabrication is truly an invaluable fortune in our group. I would like to acknowledge Yang Lin, Wei-Chang Li, Mehmet Akgul, and Tristan Rocheleau, each of whom worked with me on different aspects of this work. Their perspectives and contributions were instrumental in helping me complete the work in this report. Also, I would like to thank Henry Barrow, Turker Beyazoglu, Ruonan Liu, Thura Lin Naing, Jalal Naghsh Nilchi, Alper Ozgurluk, and Robert Schneider for their helpful suggestions during weekly group meetings.

I would like to show my deepest gratitude to my parents, Wu Gang, Ling Wei, and my grandmother Yang XiuYing, for their eternal love throughout my life. Without their encouragement and support, my dream of studying at UC Berkeley will not come true. I also owe my deepest thanks to my wife, Fangran, for her unwavering support over the years in the United States.

I want to give my special thanks to the Marvell Nanofabrication Laboratory staff. Their endless effort on tool maintenance and equipment diagnostics enabled the microfabrication platform for this work. Also, I want to thank John Huggins, Richard Lossing, Kim Ly, Dalene Schwartz Corey, and all BSAC directors for their efforts to make BSAC a perfect environment for graduate students to learn and grow professionally.

Lastly, I would like to thank DARPA, BSAC, and Samsung for the financial support of my research.

Chapter 1 Introduction

1.1. Motivation: Frequency Stability Enhancement for Oscillators

High-Q capacitive-gap transduced micromechanical resonators constructed via MEMS technology have recently taken center-stage among potential next generation timing and frequency reference devices that might satisfy present and future applications. Notably, oscillators referenced to very high Q capacitive-gap transduced MEMS resonators have already made inroads into the low-end timing market, and research devices have been reported to satisfy GSM phase noise requirements [1] [2]. Figure 1.1 presents a 61-MHz Pierce oscillator referenced to a capacitive-gap transduced wine glass disk resonator that makes GSM phase noise requirement at both close to carrier and far-from-carrier offsets, with consuming only 78 microwatts of power [3]. However, like any other oscillators, environmental fluctuations such as external vibrations, bias voltage noise, or charging, may greatly degrade this performance [4] [5].

The work in [6] on such capacitive-gap MEMS devices posted some impressively low acceleration sensitivities, with measured sensitivity vectors less than 0.5ppb/g. Interestingly, theory predicts that the acceleration sensitivity of these devices should be even better than this, if not for frequency instability due to electrical stiffness [6]. Indeed,

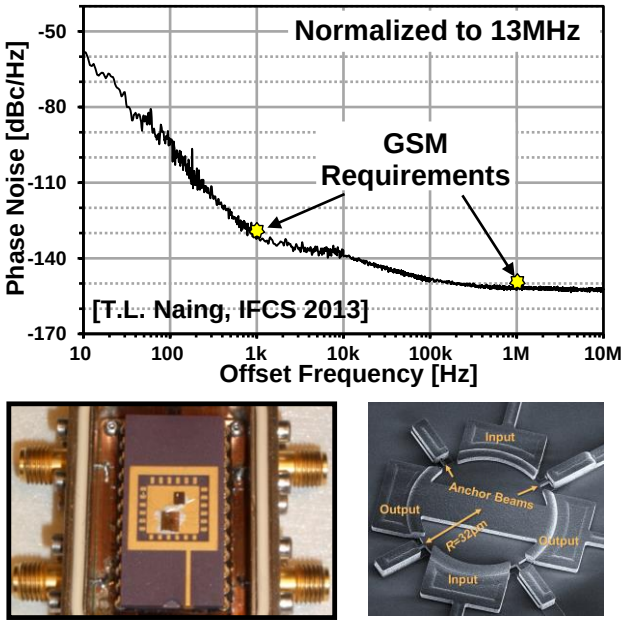

Figure 1.1. A 61-MHz Pierce oscillator referenced to a capacitive-gap transduced wine glass disk resonator with its phase noise performance making the GSM specifications.

electrical stiffness is predicted to set lower limits on not only short-term frequency stability, but long-term as well. As the electrical stiffness k_e of a capacitive-gap MEMS resonator is often determined by dc-bias voltage V_P, electrode-to-resonator overlap capacitance C_o, and the capacitive gap spacings d_o, environmental fluctuations that disturb any of these parameters will cause instability in electrical stiffness and generate frequency shift, as shown in Figure 1.2. For instance, theoretical analysis of micromechanical wine-glass disk resonators reveals that acceleration-induced changes in electrode-to-resonator gap spacing or overlap area that in turn induce shifts in electrical stiffness dominate among sources that shift frequency during accelerations [7]. In addition, noise or drift on the power supply manifests as fluctuations on the resonator dc-bias V_P that obviously destabilize the electrical stiffness, and thereby, resonance frequency [4].

Pursuant to suppress the electrical stiffness and enhance frequency stability, the work in this report develops a new negative capacitance based equivalent circuit model [8], which reveals that capacitive-gap transduced micromechanical resonators can offer better frequency stability against environment fluctuations when used in large mechanically-coupled arrays [9]. The key to enhanced frequency stability is the electrode-to-resonator capacitance (C_o) generated by the parallel combination of input/output electrodes overlapping each resonator in the array that in turn reduces the efficacy of the bias voltage-controlled electrical stiffness. Here, the new equivalent circuit based on negative capacitance also provides improved visualization that helps to identify methods to suppress electrical stiffness induced frequency variation. The circuit model indicates that the most stable MEMS-based oscillators (e.g., against supply noise and acceleration) are the capacitive-gap transduced ones that utilize mechanically-coupled arrays of resonators.

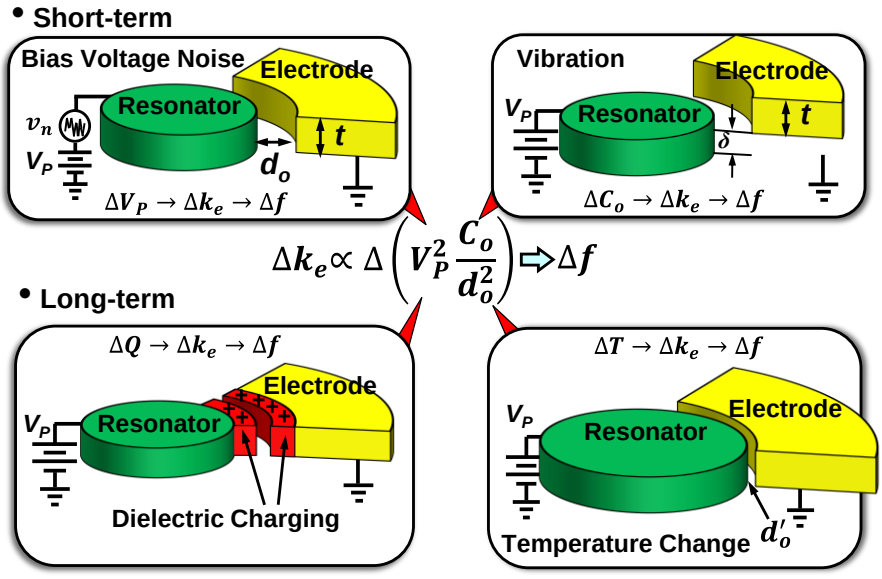

Figure 1.2. Various factors that can contribute to electrical stiffness induced frequency instability, which includes bias voltage noise, environment vibration, dielectric charging, and temperature drift.

1.2. Capacitive-gap Transduced Radial Contour Mode Disk Resonators

A capacitive-gap transduced micromechanical resonator usually consists of a suspended mechanical structure and capacitive transducers that convert energy between electrical domain and mechanical domain. It generally offers the best quality factor among different types of micromechanical resonators (which is desired for low phase noise oscillator applications) [10] [11], since they generally are constructed in single high quality materials, and thus suffer less from the material interface losses that can encumber other transducer types (e.g., piezoelectric). Figure 1.3 compares the quality factor of a capacitive-gap transduced disk resonator and a piezoelectric ring resonator at similar frequencies around 500 MHz [12] [13]. The capacitive-gap transduced disk resonator achieved 10× higher Q compared with the piezoelectric resonator. Although piezoelectric transducers may be more successful in achieving lower impedances between 50 Ω and 377 Ω for matching to off-chip wireless components [14], capacitive-gap transduced devices can scale down their impedances by using some of the recent developed techniques [15] [16]. In addition to better Q, capacitive-gap transduced resonators also offer more flexible geometries with CAD-definable frequencies, as they can take the form of many shapes, such as beams, disks, rings, or plates [17] [18] [10] [19], and their frequencies usually depend on lateral geometries that can be defined by lithography, which enables the fabrication of multi-frequency devices on a single chip.

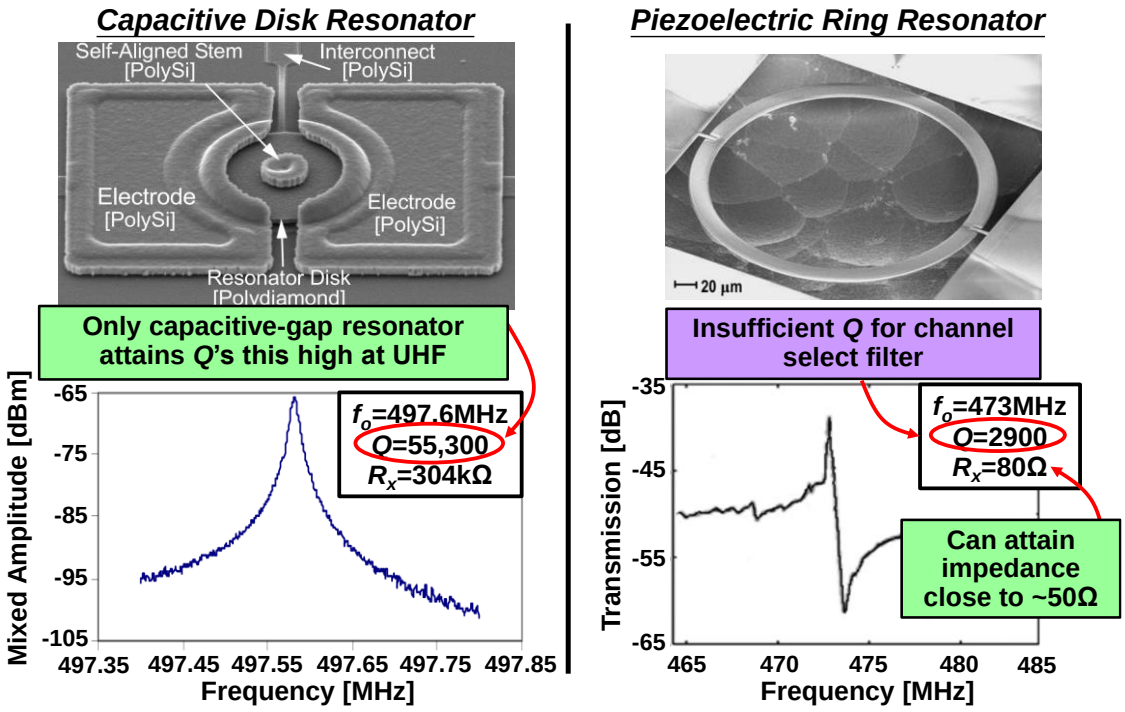

Figure 1.3. Q Comparison between a capacitive-gap transduced disk resonator and a piezoelectric ring resonator at similar resonance frequencies.

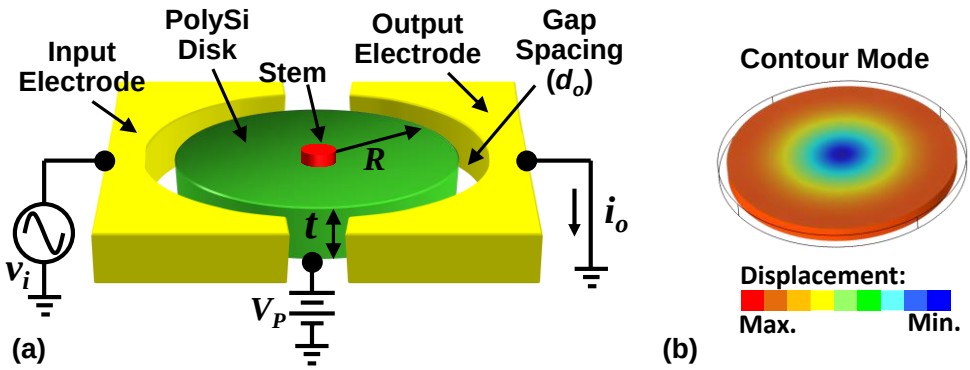

Figure 1.4. (a) Schematic of a capacitive-gap transduced all-polysilicon radial contour mode disk resonator in a two-port excitation and sensing configuration; (b) Finite element simulation of radial contour mode shape.

Figure 1.4(a) depicts a capacitive gap all-polysilicon contour mode disk type resonator that will be discussed in this work in a typical bias, excitation, and detection scheme. This device comprises a 2μm-thick disk surrounded by two closely spaced (d_o = 50 nm) electrodes and supported by an anchored stem attached at the center of the disk, where the radial displacement is minimized in radial contour mode shape shown in Figure 1.4(b), making this attachment location a quasi-nodal point ("quasi", since the stem has finite radius).The device is excited into resonance via a combination of a dc-bias voltage V_P applied to the conductive polysilicon resonant structure and an ac signal v_i applied to the input electrode, which together induce a force at the frequency of v_i that drives the disk into resonance vibration when the frequency of v_i matches the resonance frequency. Once vibrating, the V_P-biased time varying capacitance between the disk and its output electrode generates an output current detectable by measurement instrumentation. The resonance frequency of a radial contour mode disk resonator can be expressed by:

$$f_o = \frac{1}{2\pi}\sqrt{\frac{k_r}{m_m}} \propto \frac{1}{R}\sqrt{\frac{E}{\rho}} \tag{1}$$

where k_r, m_m, R, E, and ρ represent the equivalent stiffness, dynamic mass, disk radius, material Young's modulus, and density of disk structure, respectively.

1.3. Traditional Equivalent Circuit

To conveniently model and simulate the behavior of a micromechanical radial contour mode disk resonator in a way that facilitates circuit analysis, Figure 1.5 presents a traditional ac small-signal electrical equivalent circuit that includes a core *lcr* tank to model the mechanical vibration, a variable capacitor to model the dependence of resonance frequency on electrical stiffness k_e, and a pair of transformers to represent the electromechanical couplings.

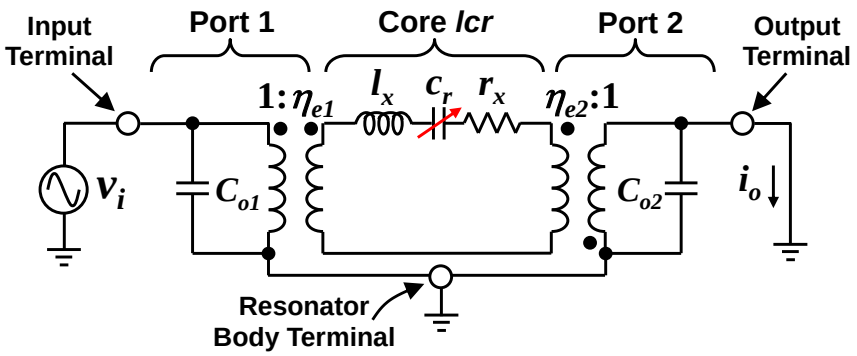

Figure 1.5. Classic equivalent electrical circuit for a capacitive gap micromechanical disk resonator with electrical stiffness lumped into the variable capacitance c_r.

1.3.1. Core *lcr* Tank

Despite its mechanical nature, the disk resonator of Figure 1.4(a) still looks like an electrical device when looking into its ports, and so can be modeled by the electrical inductor-capacitor-resistor (*lcr*) equivalents shown in Figure 1.5. Expressions for the element values in the *lcr* equivalents take the form:

$$l_x = m_m, c_r = \frac{1}{k_r} = \frac{1}{k_m - k_e}, r_x = b_m \tag{2}$$

where m_m, k_r, k_m, k_e and b_m are the actual values of dynamic mass, equivalent stiffness, mechanical stiffness, electrical stiffness, and damping constant of the resonator being modeled at the core *lcr* location. For radial contour mode shape with all points on the sidewalls of the disk moving the same amount, the perimeter of the disk structure usually becomes the core *lcr* location. The equivalent mass can be obtained by dividing the total kinetic energy KE_{tot} by one-half the square of the velocity at the core *lcr* location [18]. Doing so on the perimeter of the disk yields:

$$m_m = \frac{KE_{tot}}{\frac{1}{2}v^2(R,\theta)} = \frac{2\pi\rho t \int_0^R r J_1^2(hr)dr}{J_1^2(hR)} \tag{3}$$

where ρ, t, and R are the material density, thickness, and radius of the disk structure; $J_n(hr)$ is the Bessel function of the first kind of order n; and h is a constant defined by Young's Modulus E, density ρ, Poisson ratio ν of the disk material, and radian resonance frequency ω_o:

$$h = \sqrt{\omega_o^2 \rho / \left(\frac{2E}{2+2\nu} + \frac{E\nu}{1-\nu^2}\right)} \tag{4}$$

From (2) and (3), expressions for l_x, c_r, and r_x in the *lcr* tank at a location on the disk perimeter can be obtained using the following relations [18]:

$$l_x = m_m \tag{5}$$

$$c_r = \frac{1}{\omega_o^2 m_m} \tag{6}$$

$$r_x = \frac{\omega_o m_m}{Q} \tag{7}$$

1.3.2. Electromechanical Coupling Factor η_{ei}

As the *lcr* tank only captures the mechanical behavior of the disk structure, this equivalent circuit also needs a transformer to model the transduction from mechanical domain to electrical domain or vice versa. A succinct derivation of the transformer turn ratio η_{ei}, which is also called the electromechanical coupling factor, follows directly from consideration of the mechanical forces generated by voltages applied to terminals of the disk resonator depicted in Figure 1.4(a). A dc-bias voltage V_P on the resonator body and an ac voltage signal v_i at the input together generate an electrostatic input force F_i in a radial direction that takes the following form:

$$F_i = \frac{1}{2}\frac{\partial C_i}{\partial r}(V_P - v_i)^2 \tag{8}$$

where C_i represents the electrode-to-resonator overlap capacitance when the disk moves *r* in radial direction, and $\partial C_i/\partial r$ is the change in electrode-to-resonator overlap capacitance per unit radial displacement at each corresponding port. Retaining only the dominant term in (8) at resonance frequency yields:

$$F_i \approx -V_P\left(\frac{\partial C_i}{\partial r}\right)v_i = -\eta_{ei}v_i \tag{9}$$

A first order approximation for $\partial C_i/\partial r$ can be obtained from the Taylor expansion of the C_i expression as follows [18]:

$$C_i(r) = C_{oi}\left(1 - \frac{r}{d_o}\right)^{-1} \rightarrow \frac{\partial C_i}{\partial r} = \frac{C_{oi}}{d_o}\left(1 - \frac{r}{d_o}\right)^{-2} \approx \frac{C_{oi}}{d_o} \tag{10}$$

which leads to the expression of electromechanical coupling factor η_{ei} as:

$$\eta_{ei} \approx \frac{V_P C_{oi}}{d_o} \tag{11}$$

1.3.3. Frequency Pulling Effect from Electrical Stiffness k_e

Because the electrode-to-resonator capacitance is a nonlinear function of the disk radial displacement, as indicated in (10), there are actually many more force components generated than represented in (9). In particular, Taylor expanding (10) further to the second term yields the electrostatic input force F_i as:

$$\begin{aligned} F_i &= \frac{1}{2}\cdot\frac{C_{oi}}{d_o}\left(V_P^2 - 2V_p v_i + v_i^2 + \frac{2V_P^2 r}{d_o} - \frac{4V_P v_i r}{d_o} + \frac{2v_i^2 r}{d_o}\right) \\ &= \frac{1}{2}\cdot\frac{C_{oi}}{d_o}\left(\ldots - 2V_p v_i + \frac{2V_P^2 r}{d_o} + \frac{2v_i^2 r}{d_o} + \cdots\right) \end{aligned} \tag{12}$$

where the last form includes only terms that can generate components at resonance frequency. Inserting $v_i = V_i\cos\omega_o t$ and $r = \Re\sin\omega_o t$ (where the fact that the displacement r is 90° phase-shifted from v_i has been accounted for) into (12) yields:

$$F_i = -\left[\frac{V_p C_{oi}}{d_o} V_i\cos\omega_o t - \left(V_p^2 + \frac{V_i^2}{2}\right)\frac{C_{oi}}{d_o^2}\,\Re\sin\omega_o t\right] \tag{13}$$

At resonance, the second force term in (13) is in phase with the radial displacement. This, together with the fact that it is also proportional to the displacement r, identifies this force component as equivalent to a stiffness, but in this case, one generated via electrical means. In particular, this force component arises from the increase and decrease in electric field strength across the electrode-to-resonator gap as the gap shrinks and grows, respectively, during mechanical resonance vibration. When the disk sidewall gets close to the electrode, the force pulling it into the electrode grows, and vice versa for the other direction, i.e. it shrinks as the disk sidewall moves away from the electrode. Thus, rather than acting to oppose displacement, as is the case for mechanical stiffness, this force acts to enhance it, which effectively makes it a negative electrical stiffness at port i, with spring constant equal to:

$$k_{ei} = \left(V_P^2 + \frac{V_i^2}{2}\right)\frac{C_{oi}}{d_o^2} \approx V_P^2\,\frac{C_{oi}}{d_o^2} \tag{14}$$

where the last form assumes that V_i is much smaller than V_P—a condition for which the reader is cautioned isn't always the case, such as in micromechanical mixlers [20].

The electrical stiffnesses of all electrodes will subtract from the mechanical spring constant of the resonator at the core *lcr* location, changing the resonance frequency of a two port radial contour mode disk resonator to:

$$f_o = \frac{1}{2\pi}\sqrt{\frac{k_r}{m_m}} = \frac{1}{2\pi}\sqrt{\frac{k_m - k_e}{m_m}}$$
$$= f_{nom}\sqrt{1 - \frac{k_e}{k_m}} \tag{15}$$
$$\approx f_{nom}\left(1 - \frac{1}{2}\cdot\frac{k_e}{k_m}\right)$$

Where k_r is the effective stiffness of the disk at any point on its perimeter, k_e is the total electrical stiffness contributed by all electrodes that surround the disk, k_m is the purely mechanical stiffness, and f_{nom} is the resonance frequency of the disk structure with zero dc-bias voltage applied. The last expression in (15) uses the binomial expansion to approximate f_o for the case in which the mechanical stiffness is many times larger than any of the electrical stiffness, which is generally true for devices in this work. Rearrange of (15) yields the fractional frequency change due to electrical stiffness as:

$$\frac{\Delta f}{f_{nom}} = -\frac{1}{2}\frac{k_e}{k_m} \tag{16}$$

1.4. Outline

This report first begins in Chapter 2 with a complete development of the new negative capacitance based equivalent circuit to capture the k_e dependent resonance frequency for capacitive-gap radial contour mode disk resonators, which provides more insights into methods that can suppress such electrical stiffness induced frequency pulling effect. After introducing the method of building mechanically coupled resonator array composite to negate electrical stiffness and enhance frequency stability in Chapter 3, Chapter 4 demonstrates the frequency stability enhancement effect from micromechanical disk array composites with different number of resonators and confirms the new model accuracy by comparison with measured data that includes plots of frequency versus dc-bias voltages. Finally, Chapter 5 explores the impact that use of this equivalent circuit should have on practical applications.

Chapter 2 Negative Capacitance Based Equivalent Circuit Model

2.1. Limitations of Traditional Equivalent Circuit

Indicated by (16), the resonance frequency of a radial contour mode disk resonator will be slightly lower than the mechanical natural frequency of the disk structure, due to frequency pulling effect of the force generated by time-varying changes in electric field strength as vibration changes the parallel-plate capacitive electrode-to-resonator gap. The ratio of electrical stiffness k_e to purely mechanical stiffness k_m actually captures the magnitude of such frequency shift. By inserting the expression of parallel-plate electrode-to-resonator overlap capacitance into (14), the total electrical stiffness k_e for a two-port radial contour mode disk resonator can be calculated as:

$$k_e = \frac{V_P^2(C_{o1} + C_{o2})}{d_o^2} = \frac{V_P^2 \epsilon A}{d_o^3} \tag{17}$$

where ϵ is the permittivity of the gap material (i.e., vacuum in this case) and A is the total overlap area between the resonator and its electrodes. Changes of any variables in k_e, such as dc-bias voltage noise, capacitance variation due to mechanical vibration, or charging induced bias voltage drift, can cause frequency stability issues for capacitive-gap MEMS resonators [4] [5].

The traditional equivalent circuit in Figure 1.5 models the influence of electrical stiffness on resonance frequency via the arrow through capacitor c_r (that indicates this capacitor is tunable) and by setting the value of c_r equal to $1/(k_m - k_e)$. Although this method for capturing electrical stiffness adequately predicts the resonance frequency, it does not convey clearly to a circuit designer the impact of electrical stiffness on the overall circuit performance. Modeling the electrical stiffness in this way in fact hides some very important capacitive-gap resonator behaviors when emplaced into certain circuits. This model also encourages designers to dismiss the impact of electrical stiffness, since many designers just neglect the k_e part in the value of c_r when drawing up equivalent circuits.

To remedy the above deficiencies of the traditional equivalent circuit model, this chapter introduces a more circuit design-friendly model presented in Figure 2.1 that captures the influence of electrical stiffness on device and circuit behavior using a negative capacitance exactly equal in magnitude to the shunt static electrode-to-resonator overlap capacitance C_{oi} at each electrode terminal.

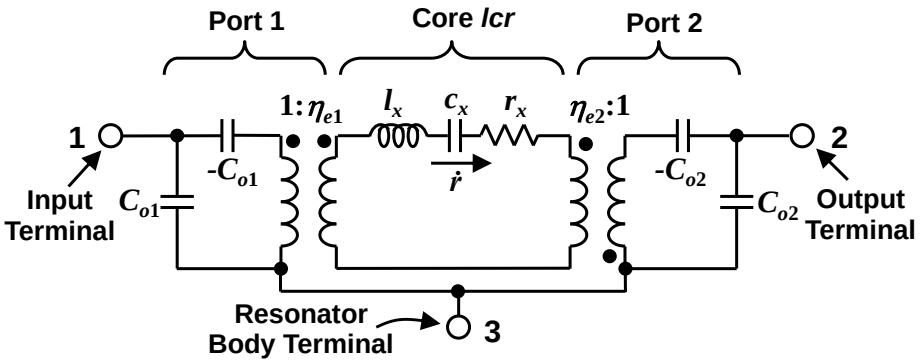

Figure 2.1. Negative capacitance equivalent circuit of a two-port micromechanical radial contour mode disk resonator. Here, the new equivalent circuit uses a negative capacitance exactly equal in magnitude to the shunt static electrode-to-resonator overlap capacitance C_{oi} at each electrode terminal to capture the electrical stiffness induced frequency shift.

2.2. Negative Capacitance Equivalent Circuit

To capture the influence of electrical stiffness more clearly, the new equivalent circuit needs to model the electrical stiffness and mechanical stiffness separately, instead of lumping them all together as shown in Figure 1.5. In general, a spring with stiffness *k* in mechanical domain can be modeled as a capacitor in electrical domain with values of *1/k*. Parallel combination of stiffness corresponds to series connection of capacitors in an equivalent electrical circuit. To attain the circuit of Figure 2.1, we start with the circuit of Figure 1.5 and first separate c_r into three capacitors: $c_x = 1/k_m$ to model the mechanical stiffness of the resonator structure, and two negative capacitors c_{ei} to model electrical stiffnesses generated at the *i* port as shown in Figure 2.2(a), which takes the following form:

$$c_{ei} = -\frac{1}{k_{e,i}} = -\frac{d_o^2}{V_P^2 C_{oi}} \tag{18}$$

where *i* denotes the corresponding port. Plugging the expression of micromechanical coupling factor η_{ei} from (11) into (18) further yields the c_{ei} expression as:

$$c_{ei} = -\frac{d_o^2}{V_P^2 C_{oi}} = -\frac{C_{oi}}{\eta_{ei}^2} \tag{19}$$

Here, c_{ei} entirely captures the electrical stiffness, allowing c_x in Figure 2.2(a) to represent purely mechanical stiffness. Further reflecting the negative capacitors c_{ei} through the transformers on both sides to outside the core *lcr* loop yields C_{ei} in the circuit of Figure 2.2 (b), where the physical shunt electrode-to-resonator capacitors C_{oi} are now matched by series negative capacitors of exactly the same values, as indicated by the following expression:

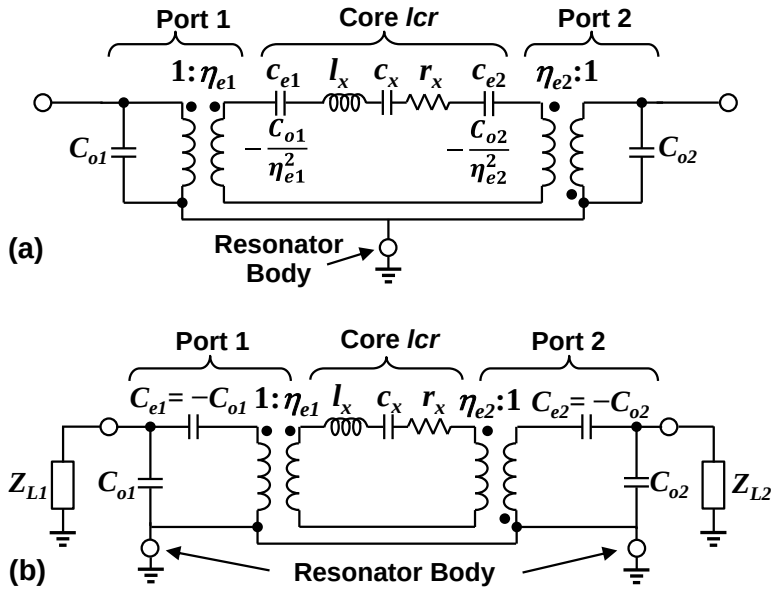

Figure 2.2. Negative capacitance small-signal equivalent circuits for a two-port capacitive-gap micromechanical contour mode disk resonator: (a) Negative capacitance equivalent circuit with electrical stiffness separated from mechanical stiffness. (b) Negative capacitance equivalent circuit with electrical stiffness reflected through transformers to outside the core *lcr* loop.

$$C_{ei} = \eta_{ei}^2 c_{ei} = -C_{oi} \tag{20}$$

Note that the resonance frequency dependency on dc-bias voltage V_P of a radial contour mode disk resonator is now entirely captured by the electromechanical coupling coefficients η_{ei}. Thus, no arrow is needed through the motional capacitor, as needed in the conventional circuit of Figure 1.5. More importantly, the value of the core c_x element stays constant, as it should. The negative C_{oi} is also a static capacitor, just like the positive C_{oi} of the physical shunt electrode-to-resonator capacitance. With this circuit, by mere inspection, a designer can now immediately see that the shunt C_{oi} presents the opportunity to effectively negate the electrical stiffness, suppress frequency changes induced by electrical stiffness, and thereby stabilize the frequency against all variables in (17)—something highly desirable in some oscillator applications.

2.3. Mitigation of Electrical Stiffness

Pursuant to determining which circuit configurations best promote k_e cancellation, Figure 2.2(b) adds load impedances Z_{Li} at each terminal. In order for the static electrode-to-resonator capacitor C_{oi} to negate the electrical stiffness represented by $-C_{oi}$, approximately same amount of current should flow through C_{oi} and $-C_{oi}$, which indicates that C_{oi} should pass most of the current flowing into the parallel combination of C_{oi} and Z_{Li}. In other words, the impedance of Z_{Li} should be much larger than that of C_{oi}, or:

$$|Z_{Li}| \gg \frac{1}{\omega_o C_{oi}} \tag{21}$$

From (21), to reduce electrical stiffness, both Z_{Li} and C_{oi} should be large. If Z_{Li} has no reactive component, operation at high frequency also suppresses electrical stiffness. However, increasing operating frequency may conflicts with application requirement because the resonance frequency is usually application oriented, which means a designer may not have the freedom to change it. In addition, as a resonator might be used with reconfigurable drive and sense circuits that present non-constant loads, it would be also challenging to achieve better frequency stability by purely relying on optimizing load impedances. These two, together, lead to the only practical choice to enhance frequency stability against electrical stiffness, which is to boost a resonator's electrode-to-resonator's overlap capacitance C_o, e.g., utilizing resonators with solid dielectric gaps [21] [22], or building array of resonators.

The work in this report focuses on coupled-array-based methods to increase C_{oi} towards better frequency stability against changes in electrical stiffness. In addition, the arraying strategy also reduces series motional resistance without degrading linearity. This is in contrast to other available approaches to increase electrode-to-resonator capacitance C_{oi}, such as reducing the electrode-to-resonator gap spacing ,and raising the effective permittivity, all of which eventually begin to degrade the device's linearity.

Chapter 3 Micromechanical Disk Array Composite

3.1. Schematic of a Radial Contour Mode Disk Array Composite

Figure 3.1(a) presents a micromechanical disk array-composite constructed by mechanically linking individual disk resonators via half-wavelength coupling beams. Here, coupling of resonators yields a coupled multi-mode system, where at each mode, all resonators vibrate at precisely the same frequency [23], allowing their outputs to be combined to boost input and output currents, thereby decreasing the motional resistance and increasing power handling. As first demonstrated in [1], the use of half-wavelength couplers both insures that all resonators vibrate in phase, as shown in Figure 3.1(b); and spreads the mode frequencies apart, making it easier to select a specific mode (when only one is wanted, e.g., in an oscillator application) by proper electrode phasing.

As described in [16], the mechanical connection of resonators in Figure 3.1(a) actually realizes a multi-pole filter structure that now has several modes of vibration. Each modal peak corresponds to a state where all resonators are vibrating at exactly the same frequency. Figure 3.2 presents finite element simulations showing the different modes of similar structure with 3 constituent resonators, which are distinguishable by the phasings between the resonators.

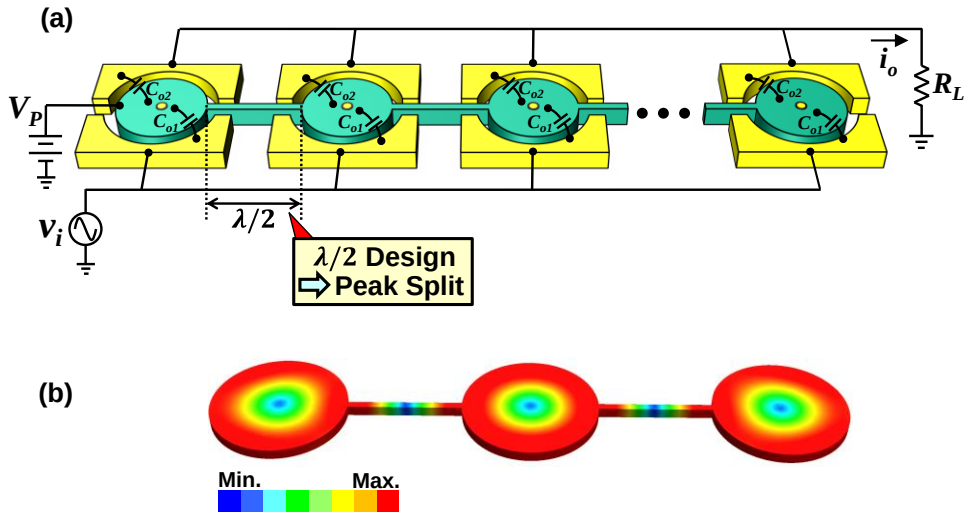

Figure 3.1. (a) Schematic of a radial contour mode disk array-composite with disks linked by λ/2 coupling beams to enforce in phase vibration of each individual resonator. (b) Simulated modal depiction of a 3-resonator disk array with all disks vibrating in phase in radial-contour mode shapes.

To only select the desired in-phase mode for a micromechanical disk array, it is advantageous to first separate other unwanted modes as far apart as possible. Since the bandwidth of a mechanical filter is proportional to the stiffness of its resonator-to-resonator coupling springs, the first step in selecting a single mode, while suppressing others, is to couple the resonators with very stiff springs. Ideally, coupling beams with lengths corresponding to half-wavelength of acoustic waves propagating in the resonator will shift the frequency of unwanted modes to infinity.

In general, a coupling beam can be modeled as an acoustic transmission line—the mechanical analog to the familiar electrical transmission line that takes the following expression:

$$\begin{bmatrix} F_1 \\ \dot{X}_1 \end{bmatrix} = \begin{bmatrix} cos(\alpha l) & jZ_m sin(\alpha l) \\ \dfrac{jsin(\alpha l)}{Z_m} & cos(\alpha l) \end{bmatrix} \begin{bmatrix} F_2 \\ \dot{X}_2 \end{bmatrix} \tag{22}$$

where F_i and $\dot{X}_i$ are the force and velocity at corresponding ports, l is the length of the coupling beam. Z_m and α in (22) are acoustic characteristic impedance and acoustic wave propagation constant, respectively, which take the forms:

$$\alpha = \frac{\omega}{\sqrt{E/\rho}}, Z_m = A_s\sqrt{E\rho} \tag{23}$$

where ω is the radian frequency of the acoustic wave, ρ is the material density, E is the Young' modulus of the beam material, and A_s is the beam cross sectional area.

Figure 3.3 shows the duality between an acoustic coupling beam and an electrical transmission line. Because the two port modeling of an electrical transmission line can be simplified by using an impedance T-network, a similar transformation can also apply on the mechanical acoustic transmission line, which generates a simplified impedance T-network model as shown in Figure 3.4 [23], with series impedance z_a and shunt impedance z_c taking the following forms:

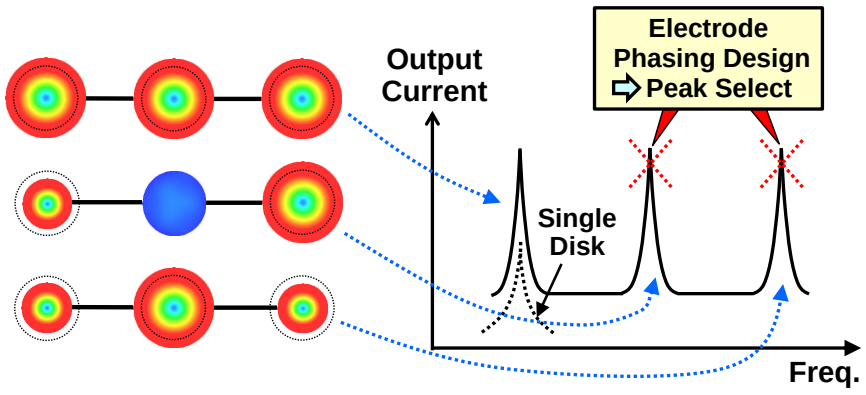

Figure 3.2. FEA simulated mode shapes of a mechanically coupled three-resonator radial contour mode disk array.

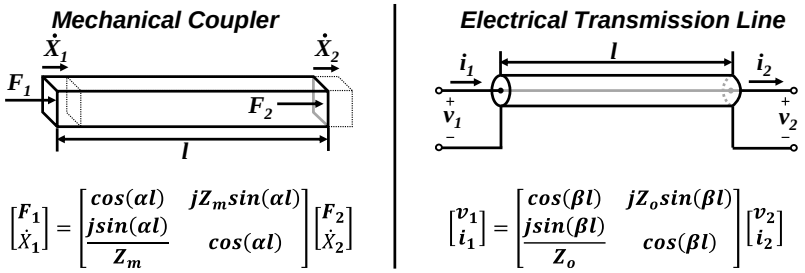

Figure 3.3. Two-port modeling of a mechanical acoustic coupling beam in analogy to an electrical transmission line.

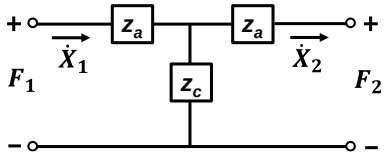

Figure 3.4. T-network modeling of a mechanical acoustic coupling beam with the force (F_i) in analogy to a voltage in electrical domain and the velocity ($\dot{X}_i$) in analogy to a current in electrical domain.

$$z_a = jA_s\sqrt{E\rho}\,tan\left(\frac{\omega}{\sqrt{E/\rho}}\cdot\frac{l}{2}\right) \tag{24}$$

$$z_c = A_s\sqrt{E\rho}/j\,sin\left(\frac{\omega}{\sqrt{E/\rho}}\cdot l\right) \tag{25}$$

The beam length of a half-wavelength coupling can be expressed as:

$$l_s = \frac{\lambda}{2} = \frac{\sqrt{E/\rho}}{2f} = \pi\frac{\sqrt{E/\rho}}{\omega} \tag{26}$$

Plugging (26) into (24)-(25) yields $|z_c| = \infty$ and $|z_a| = 0$, which makes the shunt path of Figure 3.4 an equivalent open and forces the same velocity at the two ends of the beam. It means that all resonators can only vibrate in phase with same amplitude, which effectively knocks out all other unwanted modes. It should be noted that the use of half wavelength coupling beams serves to spread the modal peaks of the filter structure in Figure 3.2 away to infinity, which facilitates the selection of one, and only one, of the modes.

In general, fabrication variations and design errors exist, which may not be able to generate exact half-wavelength coupling beams and thereby can only separate the peaks by finite distance in frequency domain. However, because each mode exhibits a unique resonator phasing, a single mode can still be selected by choosing the input ac signal and output electrode configuration to match the phasing of the desired mode, e.g. directly connecting all output electrodes together will effectively cancel the output current from the mode shape in which the center resonator keeps still and the two side resonators vibrate out-of-phase, as shown in Figure 3.2.

Once a single mode is selected, the structure practically behaves as a single resonator, but with a current handling ability equal to the sum of the currents from all constituent resonators. Thus, an *N*-resonator array can handle *N* times more power and achieve *N* times smaller motional resistance than a single resonator.

3.2. Frequency Stability Enhancement of a Disk Array Composite

Of course, this coupled array strategy not only produces a larger total output current and smaller motional resistance [16], but also attains much larger electrode-to-resonator overlap capacitors C_{oi}, and thus reduces the electrical stiffness and its associated instability, according to (21).

Because a micromechanical disk array-composite behaves like a single disk resonator when only one in-phase mode is selected, its equivalent circuit uses the same schematic and topology as that of a single disk resonator, as shown in Figure 3.5(a). For a disk array with *N* mechanically coupled disk resonators, the stiffness k_m, mass m_m, damping b_m, electromechanical coupling factor η_{ei}, and electrode-to-resonator overlap capacitance C_{oi} are all *N* times larger than for a single disk resonator. Thus, simple multiplication or division by *N* is all that is needed to derive coupled array equivalent circuit element values from those of a single disk resonator, as shown in Figure 3.5(b). Note that although the electrical stiffness goes up by *N* according to (17), so does the mechanical stiffness, so their ratio k_e/k_m remains the same and the fundamental efficacy by which k_e pulls the frequency, as governed by (15), does not increase. Instead, with C_{oi} presenting a much smaller impedance, more current flows through C_{oi} than Z_{Li}, allowing it to cancel more of C_{ei}, thereby negating the electrical stiffness induced frequency instability via circuit interaction.

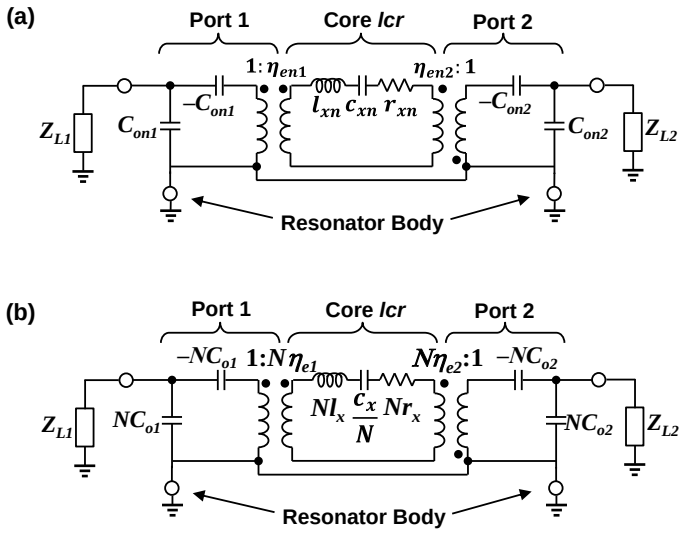

Figure 3.5. (a) Negative capacitance equivalent circuit of a disk array–composite. With only the in-phase mode selected, the structure practically behaves like a single resonator, making it share the same equivalent circuit topology as a single disk resonator. (b) Negative capacitance equivalent circuit of a disk array with *N* resonators based on element values in the single resonator equivalent circuit in Figure 2.2(b)

3.3. Design Example

Table I summarizes the needed expressions (with reference to Figure 3.5(a) for variables) while also succinctly presenting a design flow to achieve a radial-contour mode disk array with N resonators like that of Figure 3.1(a) with a specific operating frequency and with specific motional resistance R_x between its electrode terminals. The work in this report also designs several 215-MHz ($R = 12.8$ μm) radial contour mode disk arrays with various number of mechanically coupled resonators (N = 1, 8, 16, and 50), whose frequency stability enhancement effect will be analyzed in Chapter 4. Table II summarizes the design parameters, the equivalent circuit variables, and the electrical stiffness induced frequency shift for four different type of disk array designs which have the same disk radius ($R = 12.8$ μm) and coupling beam length, but different number of resonators.

Table I: Radial contour mode disk array design equations and procedure summary

Objective/Procedure	Parameter	Relevant Design Equations for a Given Parameter	Eq.
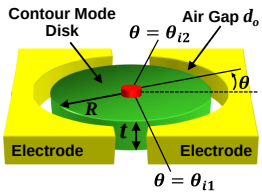	Solve For δ	$\delta \times \frac{J_0(\delta)}{J_1(\delta)} = 1 - \nu$	(27)
	Angular Resonance Frequency ω_{nom}	$\omega_{nom} = \frac{\delta}{R}\sqrt{\frac{E}{\rho(1-\nu^2)}}$	(28)
Given: ω_{nom}, V_P, N, R_{xij} (= resistance between terminals i and j). Find: R, d_o. 1. Choose E, ρ, and ν by choice of structural material. 2. Choose thickness t. 3. Use (28) to find the R needed to achieve ω_{nom}. Use (27) to get δ in the process. 4. Use (32) to find the d_o needed to achieve R_{xij}. 5. (29), (30) and (31) yield all needed values in the ac small signal equivalent circuit in Figure 3.5(a).	Core Equiv. Circuit Elements	$l_{xn} = Nm_m = N\frac{2\pi\rho t\int_0^R rJ_1^2(hr)\,dr}{J_1^2(hR)}$, $h = \sqrt{\frac{\omega_{nom}^2\rho}{(\frac{2E}{2+2\nu}+\frac{E\nu}{1-\nu^2})}}$ $c_{xn} = \frac{1}{Nk_m} = \frac{1}{\omega_{nom}^2 Nm_m}$, $r_{xn} = Nb_m = \frac{\omega_{nom}Nm_m}{Q}$	(29)
	Static Overlap Capacitor	$C_{oni} = N\frac{\epsilon_o(\theta_{i2}-\theta_{i1})Rt}{d_o}$	(30)
	Electro-mechanical Coupling Coefficient	$\eta_{eni} = V_P\frac{C_{oni}}{d_o}$	(31)
	Motional Resistance	$R_{xij} = \frac{r_{xn}}{\eta_{eni}\eta_{enj}}$	(32)

Table II: Comparison of design variables and equivalent circuit element values for 215-MHz radial contour mode disk arrays with different number of mechanically-coupled resonators.

	Parameter	Source	Number of Resonators				Units
Design Variables	Number of Resonators, N	N/A	1	8	16	50	N/A
	Disk Radius, R	Layout	12.8	12.8	12.8	12.8	μm
	DC Bias Voltage, V_P	N/A	9	9	9	9	V
	Disk Thickness, t	Fabrication	2	2	2	2	μm
	Electrode-to-Resonator Gap, d_o	Fabrication	50	50	50	50	nm
	Natural Frequency, f_{nom}	Equation (28)	215	215	215	215	MHz
	Coupling Beam Length l	Layout	21.2	21.2	21.2	21.2	μm
	Electrode Span Angle, θ	Layout	133	133	133	133	(°)
	Quality Factor, Q	Measurement/ Estimate	10,000	10,000	10,000	10,000	N/A
Equivalent Circuit Elements	Equivalent Inductance, l_{xn}	Equation (29)	1.81×10^{-12}	1.45×10^{-11}	2.89×10^{-11}	9.03×10^{-11}	H
	Equivalent Capacitance, c_{xn}	Equation (29)	3.03×10^{-7}	3.79×10^{-8}	1.89×10^{-8}	6.06×10^{-9}	F
	Equivalent Resistance, r_{xn}	Equation (29)	2.44×10^{-7}	1.95×10^{-6}	3.91×10^{-6}	1.22×10^{-5}	Ω
	Overlap Capacitance, $C_{on1} = C_{on2}$	Equation (30)	9.2	73.8	148	462	fF
	Electromechanical Coupling, $\eta_{en1} = \eta_{en2}$	Equation (31)	1.46×10^{-6}	1.17×10^{-5}	2.33×10^{-5}	7.29×10^{-5}	N/A
	Electrical Stiffness Induced Frequency Shift $(f_o - f_{nom})/f_{nom}$	Equivalent Circuit of Figure 3.5(b)	-71.3	-56.6	-38.7	-19.8	ppm

3.4. Fabrication Process

The fabrication process for the all-polysilicon contour mode disk resonator arrays of this work deviates from previous ones, such as that of [18], in that it does not use self-aligned peg-stem anchors and it employs chemical mechanical polishing (CMP) to remove electrode overhangs. The process begins with film depositions and etches identical to those of [18] to achieve the substrate isolation layer, polysilicon interconnects, and the bottom sacrificial layer. At this point, unlike previous self-aligned processes, a mask is used to define, pattern, and etch stem anchor holes into the bottom sacrificial oxide, followed by a 2-μm LPCVD in-situ doped polysilicon film that fills the holes to form the stems and serves as the resonator structural material. Here, an AMSL300 DUV Stepper is used to realize very precise alignment, with less than 100nm error—good enough to achieve Q's comparable to those of devices with self-aligned stems.

After depositing an oxide hard mask over the structural polysilicon, disk devices and coupling links are patterned and etched as before, the gap-defining sacrificial sidewall oxide spacer is deposited, electrode to interconnect contact vias are etched, and the polysilicon electrode material LPCVD'ed 3-μm thick, all to yield the cross-section of Figure 3.6(a). At this point, the process again deviates from that of [18] in that before patterning and etching the electrodes, the top polysilicon is first CMP'ed down to the hard

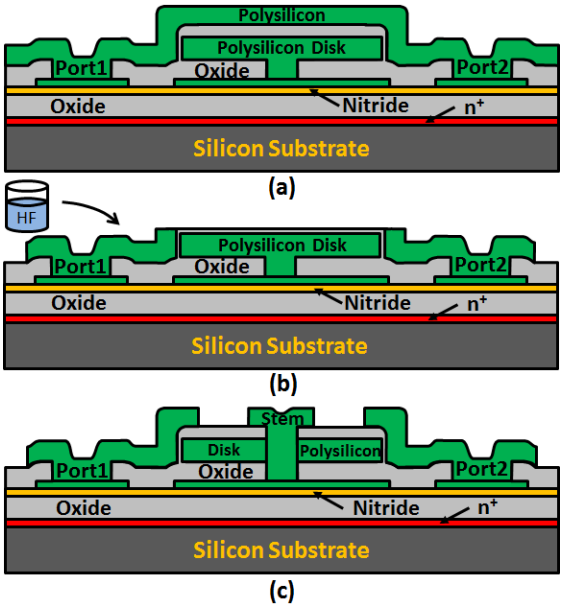

Figure 3.6. Cross-sections showing the last few steps in the fabrication process for a 215-MHz all-polysilicon disk resonators with CMPed electrodes (a. b), and a comparison to previous work's fabrication process, (c).

mask. This step removes the electrode overhangs of Figure 3.6(a), achieving the final cross section of Figure 3.6(b). When compared to the previous cross section of [11], cf. Figure 3.6(c), this new process greatly increases the pull-in voltage of these devices, where contact between the disk and the electrode overhang is often the first to occur when dc-bias voltages increase. As before, devices are released in 49 wt. % hydrofluoric acid for ~40min.

Figure 3.7 and Figure 3.8 present SEMs of fabricated 215-MHz 50-nm capacitive-gap transduced half-wavelength-coupled disk arrays employing 16 and 50 resonators, respectively, in straight line and rectangular placement configurations.

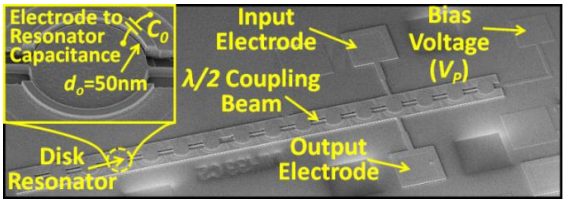

Figure 3.7. SEM of a 215-MHZ 50nm capacitive-gap contour mode disk array employing 16 resonators.

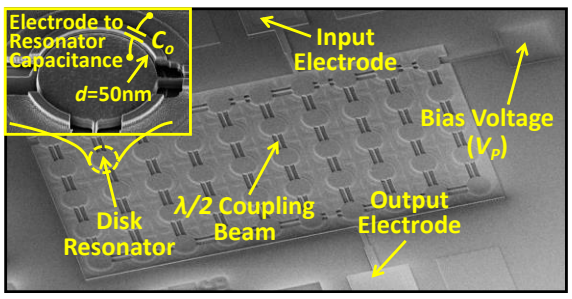

Figure 3.8. SEM of a 215-MHZ 50nm capacitive-gap contour mode disk array employing 50 resonators.

Chapter 4 Measurement Results

To gauge the degree to which arraying enhances frequency stability against dc-bias voltage changes, measured plots of frequency versus dc-bias voltage are in order, for both mechanically coupled disk array-composite resonators using various numbers of resonators, as well as for a single stand-alone disk for comparison. To this end, measurements were made under a 2μtorr vacuum environment in a Lakeshore FWPX vacuum probe station and using an Agilent E5071C network analyzer in the direct two-port excitation and sensing scheme. Figure 4.1 presents the direct two-port measurement setup used in this work for a radial contour mode disk resonator, which records the S21 parameter of the devices to observe the resonance frequency as a function of the dc-bias voltage V_P.

4.1. Frequency Stability Against DC-bias Voltages

Figure 4.2 plots the measured S21 parameter of a single radial contour mode disk resonator under different dc-bias voltage conditions (V_P = 5 V, 10 V and 15 V). It observes a 180 ppm frequency change as V_P varies from 15 V down to 5 V, which clearly shows the electrical stiffness induced frequency pulling effect. It also indicates that the frequency stability of a single disk resonator will be susceptible to all factors that changes electrical stiffness, such as environment acceleration or dc-bias voltage noise.

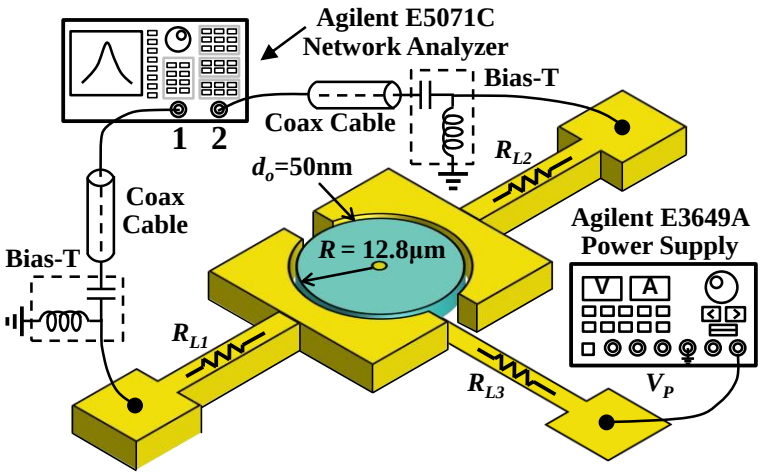

Figure 4.1. S21 direct measurement setup for a polysilicon 215-MHz capacitive-gap radial-contour mode disk resonator.

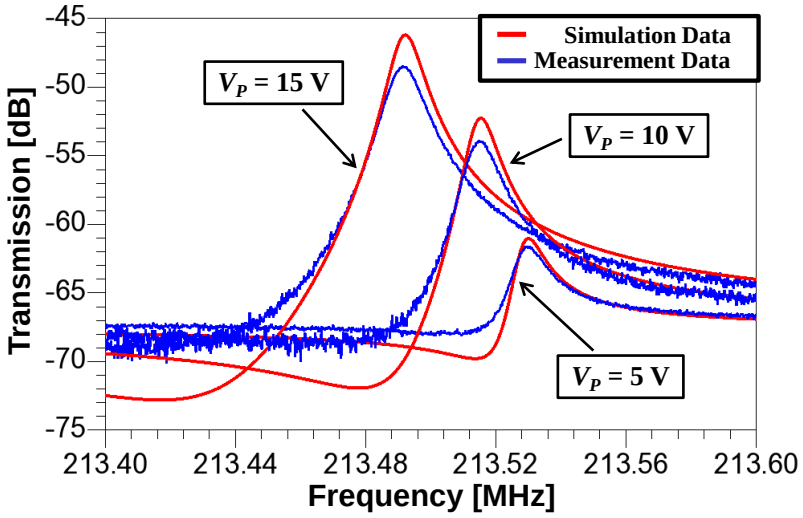

Figure 4.2. Frequency spectrum of a single radial contour mode disk resonator under different dc-bias voltage conditions. (V_P = 5 V, 10 V, and 15 V)

To demonstrate the frequency stability enhancement against dc-bias voltages from micromechanical disk array composite, Figure 4.3 plots the fractional frequency change along the *y*-axis against dc-bias voltages, for radial contour mode disk arrays with various number of resonators, e.g., N = 1, 8, 16, and 50. The measured curves clearly show a shrinking frequency dependence on dc-bias voltage as the number of resonators used in an array increases. In particular, the 50-resonator 215-MHz disk array experiences a 20 ppm frequency change when V_P varies over a 7 V span, from 2 V to 9 V, 3.5× smaller than the 70 ppm of a stand-alone device.

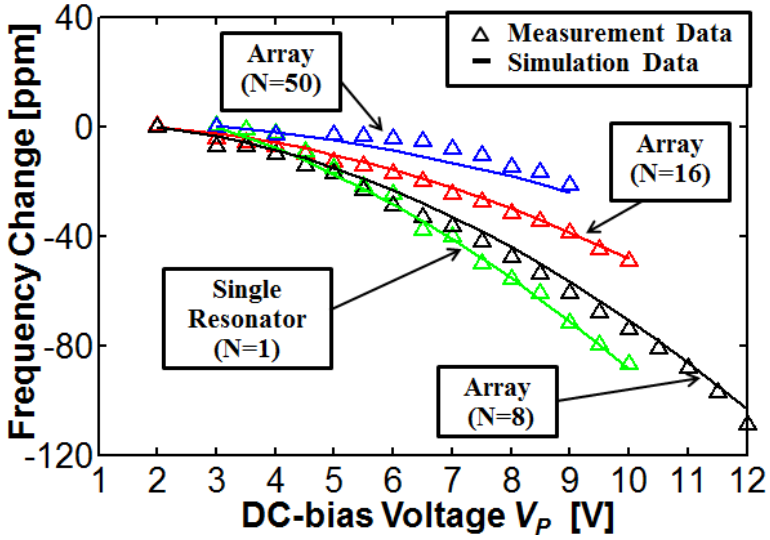

Figure 4.3. Measured curves of resonance frequency versus dc-bias voltage V_P plotted against simulation using negative capacitance equivalent circuit models for disk arrays with N=1, N=8, N=16, and N=50.

Table III: Electrode-to-resonator overlap capacitance and trace resistances for radial contour mode disk array with different number of resonators

Resonator Number (*N*)	Overlap Capacitance C_{oi} [fF]	$R_{Li,tot}$ [kΩ]
1	9.2	1.56
8	73.8	4.04
16	148	5.24
50	462	2.92

To confirm the validity of the negative capacitance equivalent circuit of Figure 3.5(b), simulated plots using this circuit are also included in Figure 4.3, showing very good agreement between theory and measurement. These simulations assume the load impedance Z_{Li} derives from a combination of series trace resistance R_{L1} and R_{L2} from input/output electrode leads, as well as similar lead resistance R_{L3} from the V_P port, all shown in Figure 4.1. Since probe coax and bond pad capacitance are nulled by calibration, the Z_{Li} in these measurements is mainly resistive. It should be noted that the total equivalent load resistance $R_{Li,tot}$ of a disk array in this work is generally larger than that of a single resonator and actually increases with the number of disks in the array. This comes about because, at least in the current layout, the distance between the V_P pad and the furthest resonator increases as the number of resonators increases, as seen from Figure 3.7, resulting in a corresponding increase in series resistance R_{L3}. Table III summarizes overlap capacitance and equivalent load resistance values for disk arrays with *N*=1, 8, 16, and 50, clearly showing larger values as the number of resonators increases, at least for straight line arrays with *N*=8 and *N*=16, like that of Figure 3.7. The series resistance of the 50-resonator array depicted in Table III is actually smaller than those of the 8- and 16-resonator ones, since its layout uses a rectangular or matrix topology, rather than a straight line, so the average distance of its resonators from its V_P pad ends up being smaller.

According to (21), increases in load resistance like those in Table III should also contribute to an overall nulling of the electrical stiffness, and thereby enhance frequency stability against dc-bias voltage fluctuations. Indeed, as the number of array resonators increases, electrical stiffness erodes due to increases in both electrode-to-resonator overlap capacitance and load resistance—a double whammy effect perfectly predicted by the negative capacitance equivalent circuit.

4.2. Motional Resistance

Figure 4.4 presents the de-embedded frequency characteristics measured using two-port configurations under vacuum for a single radial contour mode disk resonator and a 50-resonator disk array. To allow for direct comparison of motional resistance, the same dc-bias voltage was applied to each device for measurement. The 50-resonator disk array achieves a motional resistance of 2.4 kΩ, which is a 28× improvement over the single disk

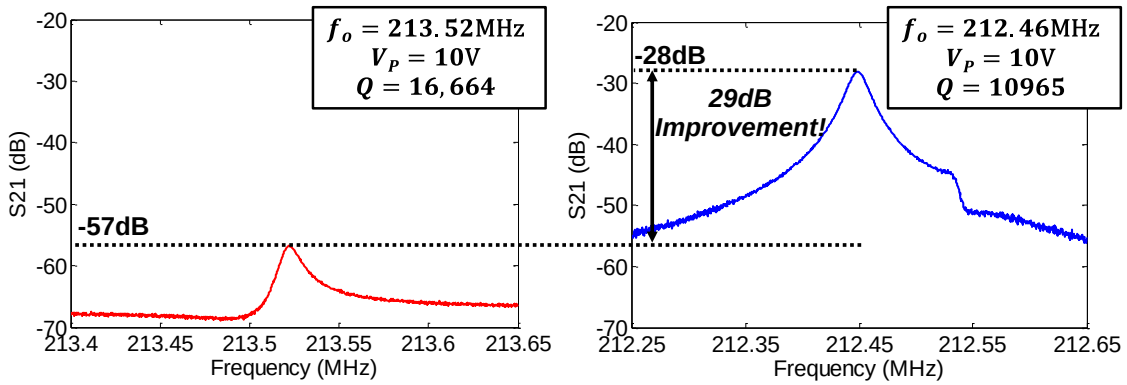

Figure 4.4. Frequency spectrum comparison of a 50-resonator radial contour mode disk array with a single disk resonator, both are measured with same dc-bias voltage.

resonator. The discrepancy between the measured 28× improvement and the predicted 50× reduction in R_x may be attributable to the fact that the 50-resonator disk array has a lower Q of 10,965, compared with the single resonator's Q of 16,664. Because of lower motional resistance, the 50-resonator disk array will suffer more Q loading effect from the trace resistance, which leads to a lower quality factor. By taking into account the Q difference, the 50-resonator disk array actually achieves 45× smaller motional resistance compared with single disk resonator, which is very close to the ideal value of 50.

Chapter 5 Conclusions

5.1. Impact on Applications

The new equivalent circuit based on negative capacitance provides improved visualization that helps to identify methods to suppress electrical stiffness induced frequency variation.

A. Reference Oscillator Design Insights

From a practical circuit perspective, the use of small source and load resistances equates to the use of voltage drive and current sensing. Conversely, the use of large source and load resistances equates to the use of current drive and voltage sensing. From the discussion in Chapter 3, voltage drive makes most sense where frequency tuning is needed, such as for a tunable filter passband application, or a voltage-controlled oscillator. On the other hand, current drive is most appropriate when frequency stability is paramount.

One example application where the choice of drive and sense type could make a big difference is that of a reference oscillator that must be stable against a variety of environmental perturbations. These include acceleration, power supply noise, drift, and undue charging (e.g., due to radiation), all of which can induce instability in the oscillator's frequency. The most significant mechanism for frequency instability caused by these particular perturbations ends up being instability in the electrical stiffness. As revealed by the negative capacitance equivalent circuit in Figure 2.2(b), frequency dependence on electrical stiffness can essentially be nulled by using a high impedance input, high impedance output sustaining amplifier. Here, high impedance is defined relative to the impedance presented by the shunt C_{oi} at the resonator I/O terminals, i.e., the resistance presented by the drive/sense circuit loading each I/O port is considered "high" when it is at least 5 times larger than $1/(sC_{oi})$. This suggests that to maximize frequency stability against environmental variations, a Pierce oscillator [24] configuration would be a better choice than the commonly used transresistance sustaining amplifier.

On the other hand, if frequency tuning is important, and slight instabilities due to environmental perturbations can be tolerated, a low impedance input, low impedance output sustaining amplifier is most suitable, such as a transresistance amplifier [25].

B. Device Design Insights

For the case where frequency stability is of most interest, the negative capacitance equivalent circuit offers a very important insight: The highest stability against changes in bias voltage or overlap capacitance comes when the positive C_{oi}'s can cancel the negative ones. It will ensure maximum stability if C_{oi} can be made much greater so that its impedance is smaller than any load resistance on a given terminal.

This simple fact now reveals several methods by which the frequency stability of a capacitive-gap transduced resonator can be maximized:

1) Utilize large arrays of resonators, perhaps mechanical coupled into array composites like that of [16] and [9]. The use of many devices increases the total input or output C_{oi} so that it swamps any terminal load resistance.
2) Utilize solid dielectric gaps, such as demonstrated in [21] and [22]. Here, simply raising the gap permittivity again raises C_{oi} so that it dominates over any terminal resistance.
3) Employ small gap spacings, which not only improves motional resistance, but also raises C_{oi} to cancel more of the electrical stiffness that is represented by $-C_{oi}$.

Needless to say, design insights like these made possible by the negative capacitance equivalent circuit that can greatly improve performance or enhance specific performance parameters over others, are quite invaluable. There are sure to be many other examples, from oscillators, to filters, to mixlers [20], where explicit representation of the negative capacitance in a micromechanical resonator's equivalent circuit proves instrumental to maximizing performance.

5.2. Conclusion

By explicitly modeling electrical stiffness in a capacitive-gap transduced micromechanical resonator via a negative capacitance, the equivalent circuit of this work provides designers with needed visual cues that enable them to more intelligently choose device topologies to maximize the performance of resonator applications, especially where frequency stability is paramount. The 50-resonator capacitive-gap transduced micromechanical disk array demonstrated here enables a mere 20ppm frequency change over a 7V dc-bias voltage variation−−a 3.5× reduction over a single stand-alone disk resonator counterpart. That the new negative capacitance equivalent circuit model introduced perfectly predicts this phenomenon, while also aiding circuit visualization, bodes well for its continued use in future resonator circuits for which tailored electrical stiffness strengths are desired. Indeed, the demonstrated stability enhancing attributes of mechanically-coupled arrays that make them less vulnerable to dc-bias voltage noise, dielectric charging, and external vibrations, together with already demonstrated array-derived reductions in the standard deviation of array resonance frequency [26], present strong cases for a more prevalent use of arrays in next generation MEMS-based frequency reference devices.

Bibliography

[1] Y.-W. Lin, S.-S. Li, Z. Ren and C. T.-C. Nguyen, "Low phase noise array-composite micromechanical wine-glass disk oscillator," in *Technical Digest, IEEE, International Electron Device Meeting*, Washington, DC, Dec. 5-7, 2005.

[2] V. Kaajakari, T. Mattila, A. Oja, J. Kiihamaki and H. Seppa, "Square-extensional mode single-crystal silicon micromechanical resonator for low-phase-noise oscillator application," *IEEE Electron Device Letters*, vol. 25, no. 4, pp. 173-175, Apr. 2004.

[3] T. L. Naing, T. O. Rocheleau, E. Alon and C. T.-C. Nguyen, "A 78-Microwatt GSM Phase Noise-Compliant Pierce Oscillator Referenced to a 61-MHz Wine-Glass Disk Resonator," in *the 2013 Joint UFFC, EFTF, and PFM Symposium*, Prague, Czech Republic, Jul. 21-25, 2013, pp. 562-565.

[4] M. Agarwal, K. Park, M. Hopcroft, S. Chandorkar, R. N. Candler, B. Kim, R. Melamud, G. Yama, B. Murmann and T. W. Kenny, "Effects of mechanical vibrations and bias voltage noise on phase noise of MEMS resonator based oscillators," in *19th IEEE International Micro Electro Mechanical System Conference*, Istanbul, Turkey, Jan. 22-26, 2006.

[5] G. Bahl, R. Melamud, B. Kim, S. A. Chandorkar, J. C. Salvia, M. A. Hopcroft, D. Elata, R. G. Hennessy, R. N. Candler, R. T. Howe and T. W. Kenny, "Model and observations of dielectric charge in thermally oxidized silicon resonators," *Journal of Microelectromechanical Systems*, vol. 19, no. 1, pp. 162-174, 2010.

[6] T. L. Naing, T. O. Rocheleau, Z. Ren, E. Alon and C. T. -C. Nguyen, "Vibration-insensitive 61-MHz micromechanical disk reference oscillator," in *IEEE International Frequency Control Symposium*, Baltimore, Maryland, May 22-24, 2012, pp. 276-281.

[7] B. Kim, M. Akgul, Y. Lin, W.-C. Li, Z. Ren and C. T.-C. Nguyen, "Acceleration sensitivity of small-gap capacitive micromechanical resonator oscillators," in *IEEE International Frequency Control Symposium*, Newport Beach, USA, June 1-4, 2010, pp. 273-278.

[8] M. Akgul, L. Wu, Z. Ren and C. T.-C. Nguyen, "A negative-capacitance equivalent circuit model for parallel-plate capacitive-gap-transduced micromechanical resonators," *IEEE Transactions on Ultrasonics, Ferroelectrics, and Frequency Control*, vol. 61, no. 5, pp. 849-869, Apr. 2014.

[9] L. Wu, M. Akgul, W.-C. Li, Y. Lin, Z. Ren, T. Rocheleau and C. T.-C. Nguyen, "Micromechanical disk array for enhanced frequency stability against bias voltage fluctuations," in *Joint UFFC, EFTF and PFM Symposium*, Prague, Czech, 2013.

[10] T. L. Naing, T. Beyazoglu, L. Wu, M. Akgul, Z. Ren, T. O. Rocheleau and C. T.-C. Nguyen, "2.97-GHz CVD diamond ring resonator with Q> 40,000," in *IEEE International Frequency Control Symposium*, Baltimore, MD, May 21-24, 2012, pp. 570-575.

[11] L. Wu, M. Akgul, Z. Ren, Y. Lin, W. Li and C. T.-C. Nguyen, "Hollow stems for higher micromechanical disk resonator quality factor," in *IEEE International Ultrasonics Symposium*, Orlando, FL, Oct. 18-21, 2011, pp. 1964-1967.

[12] J. Wang, J. E. Butler, T. Feygelson and C. T.-C. Nguyen, "1.51-GHz polydiamond micromechanical disk resonator with impedance-mismatched isolating support," in *17th International IEEE Micro Electro Mechanical Systems Conference*, Maastricht, The Netherlands, Jan. 25-29, 2004, pp. 641-644.

[13] G. Piazza, P. J. Stephanou and A. P. Pisano, "Piezoelectric aluminum nitride vibrating contour-mode MEMS resonators," *Journal of Microelectromechanical Systems,* vol. 15, no. 6, pp. 1406-1418, Dec. 2006.

[14] C.-M. Lin, V. Yantchev, J. Zou, Y.-Y. Chen and A. P. Pisano, "Micromachined One-Port Aluminum Nitride Lamb Wave Resonators Utilizing the Lowest-Order Symmetric Mode," *Journal of Microelectromechanical Systems,* vol. 23, no. 1, pp. 78-91, Feb. 2014.

[15] M. Akgul, B. Kim, Z. Ren and C. T.-C. Nguyen, "Capacitively transduced micromechanical resonators with simultaneous low motional resistance and Q > 70,000," in *Hilton Head Workshop*, Hilton Head Island, South Carolina, 2010.

[16] M. U. Demirci and C. T. -C. Nguyen, "Mechanically corner-coupled square microresonator array for reduced series motional resistance," *Journal of Microelectromechanical Systems,* vol. 15, no. 6, pp. 1419-1436, Dec. 2006.

[17] K. Wang, A.-C. Wong and C. T.-C. Nguyen, "VHF free-free beam high-Q micromechanical resonators," *Journal of Microelectromechanical Systems,* vol. 9, no. 3, pp. 347-360, 2000.

[18] J. Wang, Z. Ren and C. T.-C. Nguyen, "1.156-GHz self-aligned vibrating micromechanical disk resonator," *IEEE Transactions on Ultrasonics, Ferroelectrics, and Frequency Control,* vol. 51, no. 12, pp. 1607-1628, Dec. 2004.

[19] J. E.-Y. Lee, Y. Zhu and A. A. Seshia, "A bulk acoustic mode single-crystal silicon microresonator with a high-quality factor," *Journal of Micromechanics and Microengineering,* vol. 18, no. 6, 2008.

[20] A.-C. Wong and C. T.-C. Nguyen, "Micromechanical mixer-filters," *Journal of Microelectromechanical Systems,* vol. 13, no. 1, pp. 100-112, Feb. 2004.

[21] Y.-W. Lin, S.-S. Li, Y. Xie, Z. Ren and C. T.-C. Nguyen, "Vibrating micromechanical resonators with solid dielectric capacitive transducer gaps," in *IEEE International Frequency Control Symposium*, Vancouver, Canada, Aug. 29-31, 2005, pp. 128-134.

[22] D. Weinstein and S. A. Bhave, "Internal dielectric transduction in bulk-mode resonators," *Journal of Microelectromechanical Systems,* vol. 18, no. 6, pp. 1401-1408, 2009.

[23] R. A. Johnson, Mechanical Filters in Electronics, New York: Wiley, 1983.

[24] S. Lee, M. U. Demirci and C. T.-C. Nguyen, "A 10-MHz Micromechanical Resonator Pierce Reference Oscillator," in *Digest of Tech. Papers of the 11th International Conference on Solid-State Sensors & Actuators*, Munich, Germany, June 10-14, 2001, pp. 1094-1097.

[25] Y.-W. Lin, S. Lee, S.-S. Li, Y. Xie, Z. Ren and C. T.-C. Nguyen, "Series-resonant VHF micromechanical resonator reference oscillators," *IEEE Journal of Solid-State Circuits,* vol. 39, no. 12, pp. 2477-2491, Dec. 2004.

[26] Y. Lin, W.-C. Li, B. Kim, Y.-W. Lin, Z. Ren and C. T. -C. Nguyen, "Enhancement of micromechanical resonator manufacturing precision via mechanically-coupled arraying," in *IEEE International Frequency Control Symposium*, Besancon, France, Apr. 20-24, 2009, pp. 58-63.